H I scale height in spiral galaxies

Narendra Nath Patra ⬛★

Raman Research Institute, C. V. Raman Avenue, Sadashivanagar, Bengaluru 560080, India

ABSTRACT

We model the galactic discs of seven nearby large spiral galaxies as three-component systems consist of stars, molecular gas, and atomic gas in vertical hydrostatic equilibrium. We set up the corresponding joint Poisson–Boltzmann equation and solve it numerically to estimate the 3D distribution of H I in these galaxies. While solving the Poisson–Boltzmann equation, we do not consider a constant H I velocity dispersion (σ_{HI}); rather, we develop an iterative method to self-consistently estimate the σ_{HI} profile in a galaxy by using the observed second-moment profile of the H I spectral cube. Using the density solutions, we determine the H I vertical scale height in our galaxies. We find that the H I discs flare in a linear fashion as a function of radius. H I scale height in our galaxies is found to vary between a few hundred parsecs at the centre to $\sim$1–2 kpc at the outskirts. We estimate the axial ratio of the H I discs in our sample galaxies and find a median ratio of 0.1, which is much lower than what is found for dwarf galaxies, indicating much thinner H I discs in spiral galaxies. Very low axial ratios in three of our sample galaxies (NGC 5055, NGC 6946, and NGC 7331) suggest them to be potential superthin galaxies. Using the H I distribution and the H I hole sizes in NGC 6946, we find that most of the H I holes in this galaxy are broken out into the circumgalactic medium and this breaking out is more effective in the inner radii as compared to the outer radii.

Key words: atomic data – galaxies: ISM – galaxies: kinematics and dynamics – galaxies: spirals – galaxies: structure – radio lines: ISM.

1 INTRODUCTION

The atomic hydrogen (H I) in galaxies is one of the most critical components which directly influences the physical, chemical, and dynamical evolution of a galaxy. The atomic gas acts as a long-term fuel for star formation and found to correlate with the current star formation in both spiral and dwarf galaxies (Kennicutt 1998; Bigiel et al. 2008; Roychowdhury et al. 2009; Leroy et al. 2009; Roychowdhury et al. 2015; Patra et al. 2016; Bacchini et al. 2019a, b). Though the stars born out of molecular beds, the molecular gas forms out of the cold neutral medium (CNM) phase of the interstellar medium (ISM). The connection between the ISM phases and the star formation requires the knowledge of the density distribution of the H I in galaxies, which might play a pivotal role in deciding different phase transitions and inducing instabilities (Toomre 1964; Madore 1977; Burton 1987; Wolfire et al. 1995; Alves, Lombardi & Lada 2007). In fact, in a recent study, Bacchini et al. (2019a) have shown that a volumetric star formation law shows a much lower scatter than the traditional star formations laws with surface densities. This, in turn, indicates that the volume density distribution of the gas in galaxies is crucial in understanding the origin of star formation and hence, the star formation laws.

H I also plays a vital role in understanding the dynamical evolution of galaxies. For example, H I extends to much larger radii as compared to optical discs and serves as a tracer of the underlying dark matter halo potential at these regions. Such as, to date, the H I rotation curve is the most robust indicator of the presence of dark matter in

galaxies, and it is routinely used to investigate the properties of the dark matter haloes (Bosma 1978, 1981; van Albada et al. 1985; Begeman 1987; de Blok et al. 2008; Oh et al. 2015; Iorio et al. 2017). Moreover, the distribution of H I is an excellent tracer of the gravitational potential in the vertical direction as well. For example, in the Galaxy, it is observed that the H I flares as a function of the galactocentric radius. In that sense, the H I can trace the variation in the gravitational potential (and hence the underlying dark matter density) in the vertical direction (Banerjee & Jog 2008), especially on the outskirts of a galaxy where the dark matter dominates.

The 3D distribution of H I in galaxies is also crucial to many other physical properties of galaxies. For example, the thickness of the H I discs in galaxies influences the effective cross-section to the background quasars, which produces the absorption spectra. Thicker H I discs in a particular type of galaxies would also increase their incident rates as a function of redshift as well (see e.g. Zwaan et al. 2005; Patra, Chengalur & Begum 2013; Roy et al. 2013). Further, the thickness of the H I layer in a galaxy decides the size distribution of the H I holes originated due to supernovae or stellar feedback. Consequently, it determines if the H I shell would break into the circumgalactic medium (CGM) polluting it with metal-enriched gas or not (Mac Low & Ferrara 1999; Silich & Tenorio-Tagle 2001). However, despite its tremendous importance, a direct determination of the 3D distribution of the H I is difficult in external galaxies due to the line-of-sight integration effect. For the Galaxy on the other hand, determination of the H I distribution is possible with direct observations assisted with minimal modelling (Grabelsky et al. 1987; Wouterloot et al. 1990; Nakanishi & Sofue 2003; Kalberla & Dedes 2008; Rathborne et al. 2009; Roman-Duval et al. 2010, 2016; Sofue 2017; Marasco et al. 2017). For external galaxies, using observation

only, a direct estimation of the vertical H I distribution [and hence the H I scale height (defined as the half width at half-maxima, HWHM, of the vertical density distribution)] without modelling is only possible if the galaxy has a constant vertical scale height and, viewed at an edge-on orientation. However, for almost no galaxies, the H I vertical scale height is constant as a function of radius. Hence, detailed modelling of the H I disc is essential to estimate the 3D distribution of H I in a galaxy.

In fact, a large number of previous studies has estimated the 3D distribution of stars and gas in a number of galaxies using detailed hydrostatic modelling considering galactic discs to be multicomponent isothermal systems (Woolley 1957; van der Kruit & Searle 1981a, b; van der Kruit 1981; Bahcall 1984b, a; Bahcall & Casertano 1984; Bahcall, Flynn & Gould 1991; Romeo 1992; Olling 1995; Narayan & Jog 2002; Abramova & Zasov 2008; Banerjee et al. 2011; Bacchini et al. 2019a, b). In early studies, Bahcall (1984b, a) assumed the stellar disc of the Galaxy to be an isothermal system in vertical hydrostatic equilibrium and solved the combined Boltzman–Poissons equation. They estimated the vertical stellar mass distribution and consequently measured the ratio of the halo to disc mass densities. They also used this method to determine the relationship between the total surface density of mass, observed luminosity scale height, and vertical velocity dispersion (Bahcall & Casertano 1984). Later, Romeo (1992) solved the hydrostatic equation assuming galactic discs to be two-component systems (stars + cold gas) to investigate the self-regulation mechanisms in determining the dynamics and structure of early normal spiral galaxies. The hydrostatic condition has further been used to investigate the shape of the dark matter haloes in galaxies by modelling the vertical H I distribution (see e.g. Olling 1995; Banerjee & Jog 2008).

In this work, we model the baryonic discs of seven nearby large spiral galaxies from The H I Nearby Galaxy Survey (THINGS, Walter et al. 2008) to estimate the 3D distribution of H I in them. We consider the galactic discs to be three-component systems consist of stars, molecular gas, and atomic gas in vertical hydrostatic equilibrium under their mutual gravity and the dark matter halo. We further set up the joint Poisson–Boltzmann equation of hydrostatic equilibrium and solve it numerically to obtain a detailed distribution of the H I in these galaxies.

To solve the Poisson–Boltzmann equation numerically, we adopt a similar strategy as used by Narayan & Jog (2002) and subsequent studies (Banerjee & Jog 2008; Banerjee, Matthews & Jog 2010; Patra et al. 2014; Patra 2018, 2019, 2020a, b; Sarkar & Jog 2018, 2019). However, most of these previous studies considered the vertical velocity dispersion of H I (σ_{HI}) to be constant for simplicity or lack of observation. Recently, in rigorous studies, Bacchini et al. (2019a, b) used a very similar technique to obtain a 3D distribution of H I, H_2, and star formation rate in a sample of 12 nearby star-forming galaxies and the Milky Way. Unlike previous studies, they extracted the vertical velocity dispersion of the gas discs as a function of the radius by performing detailed 3D tilted ring modelling of the kinematic data using ^{3D}Barolo (Di Teodoro & Fraternali 2015). However, they did not solve the hydrostatic equation fully self-consistently and ignored the gravity of the H_2 disc while solving for H I. Whereas, in this study, we solve the hydrostatic equilibrium equation self-consistently incorporating the gravity of all the disc components. We also do not assume a constant σ_{HI}; rather, we develop an iterative method by which we estimate the σ_{HI} profile in a galaxy from the observed second-moment profile (MOM2) of the H I spectral cube. In this approach, simultaneously, both the H I distribution and the σ_{HI} can be determined self-consistently in a galaxy.

2 SAMPLE

We select seven nearby spiral galaxies from THINGS (Walter et al. 2008) for which all the necessary data are available publicly. As part of the THINGS survey, a total of 34 galaxies were observed in H I with the Very Large Array (VLA) with a high spatial resolution of ∼ 6 arcsec. The sample was carefully chosen, such as to be part of a larger multiwavelength campaign. For example, THINGS galaxies are part of the Spitzer Infrared Nearby Galaxy Survey (SINGS, Kennicutt et al. 2003), which enables robust estimation of the stellar masses in these galaxies. They have the far-ultraviolet (FUV) data from the *GALEX* observations, which is useful to calculate the recent star formation in these galaxies. Moreover, the HERA CO Line Extra-galactic Survey (HERACLES, Leroy et al. 2009) also used the THINGS samples as the base to observe 18 large spiral galaxies with the 30-m IRAM telescope and mapped molecular gas in these galaxies.

Solving the Poisson–Boltzmann equation requires several essential input parameters. For every galaxy, one needs the surface density profiles of the disc components, which are primarily responsible for gravity. Here, it should be mentioned that several galaxies in the THINGS sample did not have publicly available molecular surface density profiles. As molecular gas is one of the crucial baryonic components which can significantly influence the dynamics, we exclude these galaxies from our sample. H I rotation curve and the mass model (dark matter distribution) of a galaxy are the other essential inputs to the hydrostatic equation. However, due to limitations in the observing parameters (e.g. inclination, data quality, etc.), mass modelling could not be performed in some of the THINGS galaxies (see de Blok et al. 2008, for more details). We exclude these galaxies as well from our sample. This leads to a total of eight galaxies for which all the necessary parameters are available to solve the hydrostatic equation. However, for one galaxy, NGC 3521, the H I disc shows strong warp at the outer disc (see e.g. fig. 77 of de Blok et al. 2008). This results in a varying inclination of the annular ring at a particular radius and can overestimate the observed σ_{HI} significantly. Hence, we exclude this galaxy from our sample which leads to a total seven galaxies in our sample for which we solve the hydrostatic equilibrium equation.

In Table 1, we present a few basic properties of our sample galaxies. Column (1) quotes the name of the galaxies, columns (2) and (3) present the coordinates (RA and Dec.) of the galaxies. In columns (4) and (5), we show the distances to the galaxies and the absolute blue-band magnitude (corrected for the extinction of the Milky Way and the galaxy itself), respectively. Column (6) denotes the optical radius (r_{25}), whereas columns (7) and (8) present the average inclination and the position angle of the H I discs as obtained by a tilted-ring fitting of the H I velocity field (as obtained by de Blok et al. 2008). Finally, column (9) shows the H I mass of the galaxies, whereas column (10) depicts the global star formation rate. The data presented in this table are compiled from Walter et al. (2008).

3 MODELLING THE GALACTIC DISCS

We model our sample galaxies as three-component systems consisting of stellar, molecular, and atomic discs. We assume that all these baryonic discs are in vertical hydrostatic equilibrium under their mutual gravity in the external force field of the dark matter halo. The dark matter potential is considered here to be fixed as determined by the observed rotation curve (or mass model). In hydrostatic equilibrium, the gravity will be balanced by the pressure. The gravity on any elemental volume (in any disc component) will

Table 1. Basic properties of our sample galaxies.

| Name | RA (J2000) | Dec. (J2000) | Dist | M_B | r_{25} | i | PA | $\log M_{HI}$ | SFR |
| | (h m s) | ($^\circ$ $'$ $''$) | (Mpc) | (mag) | (arcmin) | ($^\circ$) | ($^\circ$) | ($M_\odot$) | ($M_\odot$ yr^{-1}) |
(1)	(2)	(3)	(4)	(5)	(6)	(7)	(8)	(9)	(10)
NGC 925	02 27 16.5	+ 33 34 44	9.2	−20.04	5.3	66	287	9.66	1.09
NGC 2841	09 22 02.6	+ 50 58 35	14.1	−21.21	5.3	74	154	9.93	0.20
NGC 2976	09 47 15.3	+ 67 55 00	3.6	−17.78	3.6	65	335	8.13	0.10
NGC 3198	10 19 55.0	+ 45 32 59	13.8	−20.75	3.2	72	215	10.01	0.85
NGC 5055	13 15 49.2	+ 42 01 45	10.1	−21.12	5.9	59	102	9.96	2.42
NGC 6946	20 34 52.2	+ 60 09 14	5.9	−20.61	5.7	33	243	9.62	4.76
NGC 7331	22 37 04.1	+ 34 24 57	14.7	−21.67	4.6	76	168	9.96	4.20

Note: The data presented in this table are compiled from Walter et al. (2008).

be resulted due to all the three components, whereas, the pressure would be determined only by the velocity dispersion of an individual component. For simplicity, we assume all the three baryonic discs are concentric and coplanar with the centres coinciding with that of the dark matter halo. In that case, the Poisson's equation of hydrostatic equilibrium at any radius can be written in cylindrical polar coordinate as

$$\frac{1}{R}\frac{\partial}{\partial R}\left(R\frac{\partial \Phi_{\text{tot}}}{\partial R}\right) + \frac{\partial^2 \Phi_{\text{tot}}}{\partial z^2} = 4\pi G\left(\sum_{i=1}^{3}\rho_i + \rho_h\right) \quad (1)$$

where Φ_{tot} is the total potential due to the gravity of the baryonic discs and the dark matter halo. ρ_i represents the volume density of different disc components, where i runs for stars, H I, and molecular gas. ρ_h denotes the density of the dark matter halo.

In hydrostatic equilibrium, the gradient in the potential in the vertical direction would be balanced by the gradient in pressure. This can be represented by the Boltzmann equation as

$$\frac{\partial}{\partial z}\left(\rho_i \langle\sigma_z^2\rangle_i\right) + \rho_i \frac{\partial \Phi_{\text{tot}}}{\partial z} = 0 \quad (2)$$

where σ_z represents the velocity dispersion of different baryonic discs and is a measure of the vertical pressure. Equation (2) can be used to simplify equation (1) as

$$\langle\sigma_z^2\rangle_i \frac{\partial}{\partial z}\left(\frac{1}{\rho_i}\frac{\partial \rho_i}{\partial z}\right) = -4\pi G\left(\rho_s + \rho_{HI} + \rho_{H2} + \rho_h\right)$$
$$+ \frac{1}{R}\frac{\partial}{\partial R}\left(R\frac{\partial \Phi_{\text{tot}}}{\partial R}\right) \quad (3)$$

where, ρ_s, ρ_{H2}, and ρ_{HI} are the volume densities of stars, molecular gas, and atomic gas, respectively. The rightmost term in the RHS of equation (3) originates due to the gradient of the potential in the radial direction. This can be estimated using the observed rotation curve. The H I rotation curve is expected to trace the potential of a galaxy in the mid-plane. In that sense, the radial term can be expressed as

$$\left(R\frac{\partial \Phi_{\text{tot}}}{\partial R}\right)_{R,z} = (v_{\text{rot}}^2)_{R,z} \quad (4)$$

where the v_{rot} (measured using the Doppler shift of the H I-21cm line) is implicitly taken to be equal to the circular speed. Though the above equation is strictly valid for $z = 0$, we assume that the rotation curve does not change considerably as a function of z, and it traces the potential above the mid-plane reasonably well. With this assumption, equation (3) can further be simplified using equation (4)

to rewrite the hydrostatic equilibrium equation as

$$\langle\sigma_z^2\rangle_i \frac{\partial}{\partial z}\left(\frac{1}{\rho_i}\frac{\partial \rho_i}{\partial z}\right) = -4\pi G\left(\rho_s + \rho_{HI} + \rho_{H2} + \rho_h\right)$$
$$+ \frac{1}{R}\frac{\partial}{\partial R}\left(v_{\text{rot}}^2\right) \quad (5)$$

Equation (5) represents three second-order partial coupled ordinary differential equations in $\rho_s(z)$, $\rho_{H2}(z)$, and $\rho_{HI}(z)$. The solutions of these equations at any radius would provide the density distribution, ρ_i, as a function of z. To produce a complete 3D density distribution of any disc component, one needs to solve these equations at all radii.

3.1 Input parameters

Several input parameters are required to solve equation (5) in a self-consistent manner. As the baryonic discs provide a significant amount of gravity to the hydrostatic equation, the surface density profiles play an essential input to equation (5). In Fig. 1, we show the surface density profiles of our sample galaxies. As can be seen from the figure, the stellar discs dominate the surface densities in all our sample galaxies at the inner parts whereas, the H I dominates the outskirts. It can also be seen that the molecular discs in our galaxies are considerably shorter as compared to the stellar and the H I discs. Because of this reason, at all radii, we cannot consider our galaxies as three-component systems (stars + H I + H$_2$). We, therefore, consider our galaxies to be three-component systems till the edge of the molecular discs; beyond that, we consider them to be two-component systems with stars and H I.

Another input to the hydrostatic equation is the density distribution of the dark matter halo. Particularly for H I distribution, the dark matter can play a significant role as the H I extends to regions (both in radial and vertical directions) where dark matter dominates the gravity. We use the mass models of our sample galaxies from de Blok et al. (2008) and obtain the dark matter halo parameters. The mass modelling of our sample galaxies were done using both an isothermal and an NFW halo. The NFW dark matter density profile can be given as

$$\rho_h(R) = \frac{\rho_0}{\frac{R}{R_s}\left(1 + \frac{R}{R_s}\right)^2} \quad (6)$$

whereas, the pseudo-isothermal profile (*ISO*) can be given as

$$\rho_h(R) = \frac{\rho_0}{1 + \left(\frac{R}{R_s}\right)^2} \quad (7)$$
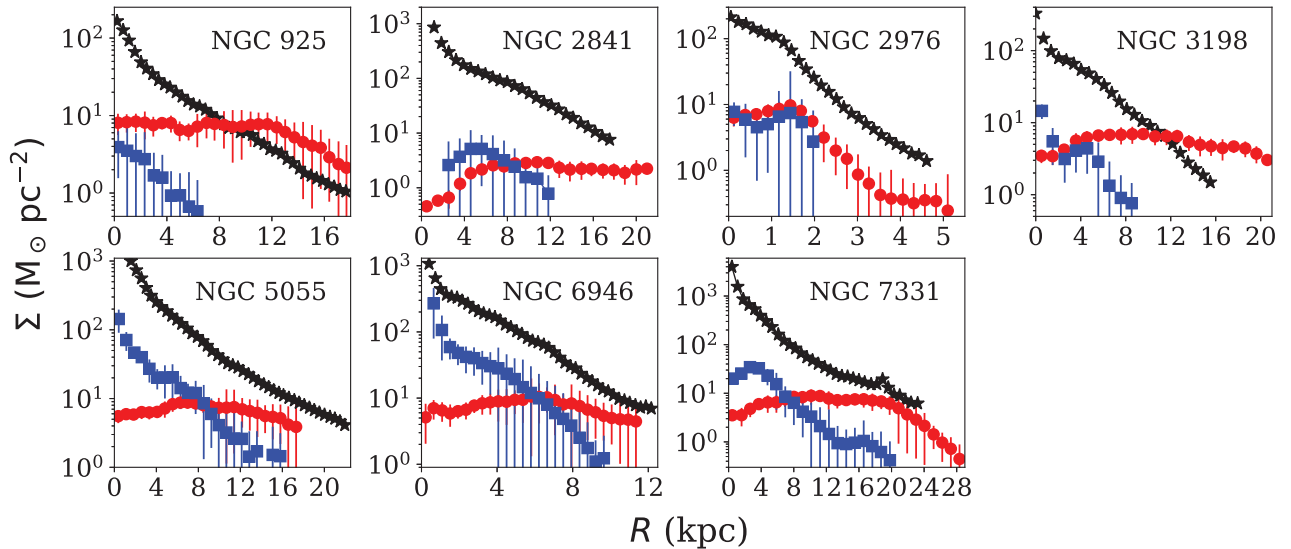
Figure 1. The surface density profiles of our sample galaxies. The black stars represent the stellar surface density profiles, whereas the red circles with error bars depict the H I surface density profiles. The molecular surface densities are shown by the blue squares with error bars. Each panel represents different galaxies, as quoted at the top right corner of the panel. The stellar surface density data weres taken from Leroy et al. (2008), whereas the H I and the molecular surface density profiles are obtained from Schruba et al. (2011).

Table 2. Dark matter halo parameters.

Galaxy	Profile	R_s (kpc)	ρ_0 ($\times 10^{-3}$ M$_\odot$pc^{-3})
NGC 925	*ISO*	9.67	5.90
NGC 2841	NFW	20.55	12.40
NGC 2976	*ISO*	5.09	35.50
NGC 3198	*ISO*	2.71	47.50
NGC 5055	*ISO*	11.73	4.80
NGC 6946	*ISO*	3.62	45.70
NGC 7331	NFW	60.20	1.05

where ρ_0 is the characteristic density, and R_s is the characteristic radius. These two parameters completely describe a spherically symmetric dark matter halo. As discussed in detail in de Blok et al. (2008, see their tables 3 and 4 for more details), no particular dark matter density profile (*ISO* or NFW) describes the rotation curves of our galaxies systematically better than the other one. Hence, depending on the galaxy, we choose a dark matter halo profile that better describes its rotation curve (based on the reduced χ^2 values of the fitted rotation curves). However, it should be noted that this choice does not influence our results significantly as both the dark matter profiles explain the rotation curves reasonably well within the observational uncertainties. In Table 2, we present the dark matter halo parameters we adopt to solve equation (5) for our sample galaxies.

The observed rotation curves are another input parameter required to evaluate the radial term in equation (5). We obtain the rotation curves of our sample galaxies from de Blok et al. (2008). In Fig. 2, we show the rotation curves of our sample galaxies. As can be seen from equation (5), the radial term is computed by calculating the first derivative of the rotation curve's square. In that case, any sudden change/jump in the rotation curve (could be due to measurement/modelling limitations), might lead to an unphysical value of the derivative and hence diverge the solutions. To overcome this shortcoming, we fit the rotation curves with a commonly used

Brandt (1960) profile. A Brandt profile can be given as

$$v_{\rm rot}(R) = \frac{V_{\rm max}\,(R/R_{\rm max})}{\left(1/3 + 2/3\left(\frac{R}{R_{\rm max}}\right)^n\right)^{3/2n}} \tag{8}$$

where $v_{\rm rot}$ is the rotation velocity, $V_{\rm max}$ is the maximum attained velocity, and $R_{\rm max}$ is the radius at which the $V_{\rm max}$ is attained. n is the index, which decides how fast or slow the rotation curve rises to $V_{\rm max}$. In Table 3, we present the fit parameters of the rotation curves. We use these parameters to calculate the radial term, which is now free from any sudden jump/variation.

The vertical velocity dispersions of the baryonic disc components are one of the most critical inputs to equation (5). The velocity dispersion alone decides the resistive force balancing the total gravity due to all the components and the dark matter halo on an elemental volume. Moreover, as gravity is coupled, the influence of a particular component's gravity is shared by all the disc components. On the other hand, the stability of a disc component (stars, molecular gas, or H I) against this combined gravity is solely controlled by its velocity dispersion. In this regard, the velocity dispersion can influence the density distribution significantly, and hence, a precise measurement of the same is essential.

Direct measurement of the stellar velocity dispersion is tough even with present-day optical telescopes. Because a direct measurement is not available, we calculate the stellar velocity dispersion analytically using the scale length of the optical disc, R_D, and the stellar surface density as described in Leroy et al. (2008, given in appendix B in their paper). In this calculation, the stellar disc is assumed to be a single-component system in hydrostatic equilibrium. As this calculation ignores gas gravity, the calculated stellar velocity dispersion is slightly underestimated.

Unlike the stellar velocity dispersion, the gas velocity dispersion can be estimated relatively easily using spectroscopic observations by radio telescopes. In the context of the molecular velocity dispersion in the Galaxy, early observations by Stark (1984) reveal that low-mass molecular clouds have a velocity dispersion of ∼9 km s^{-1}, whereas, the high-mass clouds have a relatively lower velocity dispersion of
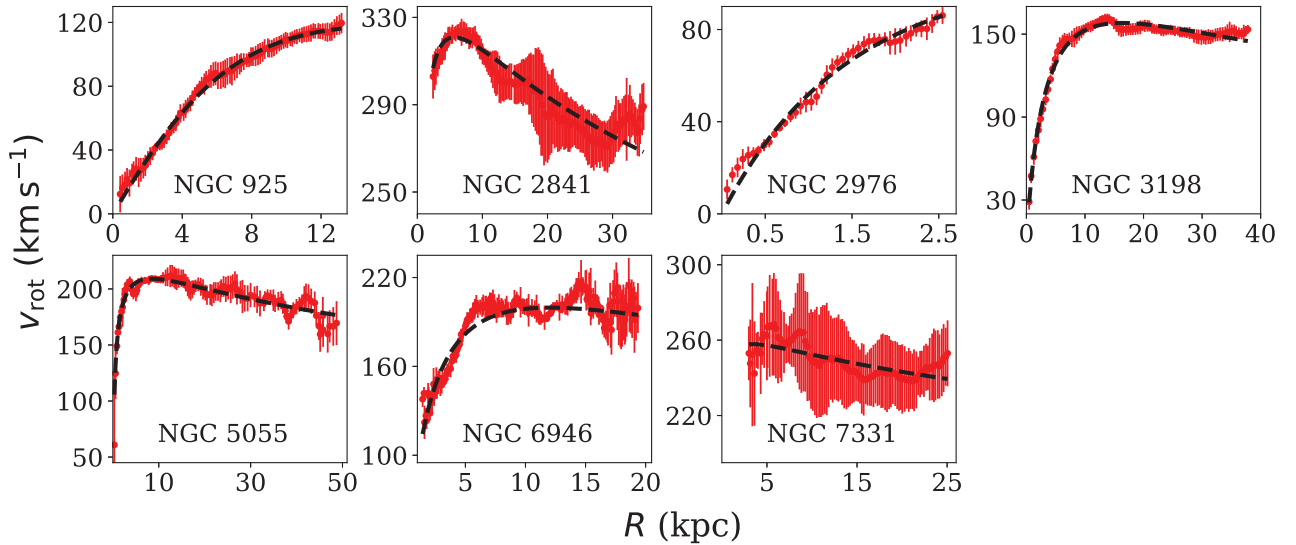
Figure 2. The rotation curves of our sample galaxies as obtained from de Blok et al. (2008). The solid red circles with error bars represent the rotation curves as obtained by a tilted-ring fitting of the H I velocity fields. The black dashed lines in each panel represent a Brandt profile fit to the rotation curves. See the text for more details.

Table 3. Best-fitting parameters of the rotation curves.

Galaxy	V_{max} (km s^{-1})	R_{max} (kpc)	n
NGC 925	118.0 ± 1.4	16.4 ± 0.9	1.80 ± 0.10
NGC 2841	320.9 ± 0.5	5.7 ± 0.2	0.36 ± 0.02
NGC 2976	103.5 ± 13.6	6.9 ± 3.0	1.05 ± 0.28
NGC 3198	158.1 ± 0.7	16.4 ± 0.3	0.82 ± 0.03
NGC 5055	209.1 ± 0.6	8.5 ± 0.2	0.36 ± 0.01
NGC 6946	199.7 ± 0.5	12.0 ± 0.6	0.69 ± 0.05
NGC 7331	257.8 ± 1.7	3.5 ± 1.3	0.12 ± 0.04

∼6.6 km s^{-1}. It should be mentioned here that the gas velocity dispersion refers to the dispersion due to the relative turbulent motions between the gas clouds. The thermal velocity dispersion (due to the kinetic temperature) within a molecular cloud is expected to be much less (∼ 0.1 km s^{-1}). In a more recent study, Caldú-Primo et al. (2013) used the data from the THINGS and the HERACLES survey for 12 nearby spiral galaxies to estimate the velocity dispersion of H I and CO. Using a spectral stacking method (for improved signal-to-noise ratio, S/N), they found $\sigma_{\mathrm{HI}}/\sigma_{\mathrm{CO}} = 1.0 \pm 0.2$ with a median $\sigma_{\mathrm{HI}} = 11.9 \pm 3.1$ km s^{-1}. Later, Mogotsi et al. (2016) used the same sample to investigate the individual high S/N spectra and found a $\sigma_{\mathrm{HI}}/\sigma_{\mathrm{CO}} = 1.4 \pm 0.2$. They concluded that the molecular disc has a diffuse component with somewhat higher velocity dispersion, which is not detected in individual spectra, but only recovered when multiple spectra are stacked. This indicates that the dominant component in the molecular disc, which is detected in individual spectra, has a velocity dispersion of ∼ 7 km s^{-1}. Hence, for our sample galaxies, we adopt a velocity dispersion of 7 km s^{-1} for their molecular discs. However, in a recent study, Marasco et al. (2017) have found a somewhat lower velocity dispersion (4.4 ± 1.2 km s^{-1}) of the molecular gas in the Galaxy inside the solar cycle. Nevertheless, the velocity dispersion of the stellar discs or the molecular discs does not influence the density distribution of H I considerably (see e.g. Banerjee et al. 2011; Patra 2019). Hence, our adopted velocity dispersions for the stellar and the molecular discs are adequate for solving equation (5).

Unlike the stellar and the molecular velocity dispersions, the H I velocity dispersion plays a crucial role in deciding the density distribution in an H I disc. Hence, careful estimation of the same is essential while solving equation (5). Early spectroscopic studies with a low spatial resolution reveal an H I velocity dispersion (σ_{HI}) in the range 6–13 km s^{-1} in nearby galaxies (Shostak & van der Kruit 1984; van der Kruit & Shostak 1984; Kamphuis & Sancisi 1993). However, more recent studies used high spatial resolution spectral cubes to estimate σ_{HI} in nearby large spiral galaxies. For example, in an extensive analysis of the second-moment (MOM2) of the H I spectral cubes from the THINGS data, Tamburro et al. (2009) found a significant variation in σ_{HI} within a galaxy as well as across the galaxies. They found a mean σ_{HI} of ∼10 km s^{-1} at the optical radius, r_{25}. These results suggest that the σ_{HI} might have a significant variation within and across our sample galaxies.

To estimate the H I velocity dispersion, we use the publicly available moment maps of our sample galaxies as obtained in the THINGS survey.[1] We refer the readers to Walter et al. (2008) for a detailed description of generating the moment maps from the observed H I spectral cubes. In Fig. 3, we show an example MOM2 map of a representative galaxy, NGC 925, from our sample. As can be seen from the figure, MOM2 in NGC 925 shows considerable variation across the galaxy. To capture this variation as a function of radius and to obtain an MOM2 profile, we construct a number of annuli as a function of the radius with a width of ∼2 times the spatial resolution. In Fig. 3, we show one such annulus with red ellipses at a radius of 10 kpc. We generate an MOM2 profile by averaging all the MOM2 values within an annulus as a function of the radius. In Fig. 5, the first panel shows the resulting MOM2 profile (solid red circles with error bars) for NGC 925.

It should be noted that due to the low S/N, some of the pixels in Fig. 3 are blanked while producing the moment maps (see Walter et al. 2008 for more details). We exclude these pixels while estimating the average MOM2 value within an annulus. Nevertheless, this has no considerable effect on our estimation of MOM2 profiles

[1] https://www2.mpia-hd.mpg.de/THINGS/Data.html
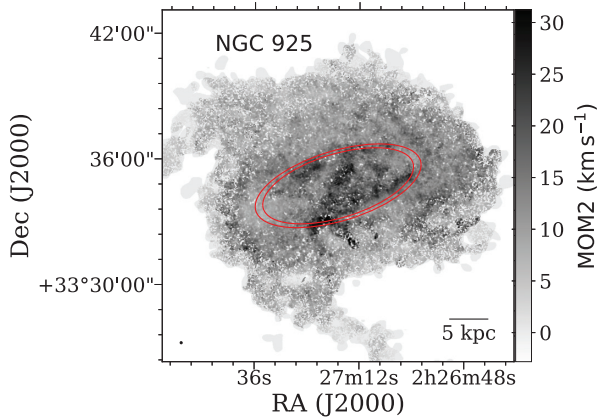
Figure 3. The MOM2 map of a representative galaxy, NGC 925 in our sample. The grey scale indicates the MOM2 distribution in the galaxy. We extract the MOM2 profile of our galaxies by averaging the MOM2 values in radial bins. The red ellipse represents a radial bin at 10 kpc distance from the centre. The solid circle at the bottom left corner represents the observing beam. Whereas, the scale bar at the bottom right represents a linear scale of 5 kpc at the distance of the galaxy, 9.2 Mpc.

as the fraction of these blanked pixels is small. However, a low S/N (especially at the outskirts of the galaxies) can have a non-negligible effect on the determined MOM2 profile of a galaxy. At low S/Ns, the MOM2 only traces the peaks of the H I profiles and hence, artificially underestimates the actual σ_{HI}. We find that the MOM2 could underestimate the σ_{HI} by ~ 10 per cent in a region where S/N is $\lesssim 3$ in MOM0 map. This value reduces to a few per cent when the S/N increases to $\gtrsim 5$. For our galaxies, we found the observed S/N to be $\gtrsim 3$ in the regions of our interests. Hence, we include a conservative error of 10 per cent in our estimated MOM2 values. Further, to account for the variation of the MOM2 within an annulus, we add the normalized (by the square root of the number of independent beams within an annulus) standard deviation in quadrature to the error bars. As can be seen from Fig. 5, the MOM2 profiles for our sample galaxies do not remain constant, rather vary considerably as a function of radius.

However, MOM2 does not represent the intrinsic velocity dispersion; instead, it is the intensity weighted σ_{HI} along a line of sight. For galaxies where the beam-smearing of line-of-sight H I spectra is significant, the MOM2 can considerably differ from σ_{HI}. Especially in the central regions of galaxies, where the gradient of the rotation curve is high. Three primary factors mainly influence the smearing of the rotational velocity into the H I spectral width. First, the slope of the rotation curve, secondly the spatial resolution, and thirdly the inclination of the H I disc. The thickness of the H I disc also can contribute to the smearing, albeit on a minor level. Due to these smearing effects, the MOM2 would always be an overestimate of the intrinsic σ_{HI} profile. Hence, using the MOM2 profile in equation (5) as input σ_{HI} is not suitable. Instead, we use an iterative method to estimate the intrinsic σ_{HI} profile in a self-consistent manner using the observed MOM2 profile. The details of this method are explained in the next section.

4 SOLVING THE HYDROSTATIC EQUATION

Equation (5) is a second-order ordinary coupled partial differential equation, which cannot be solved analytically even for a two-component system. Hence, we adopt a numerical approach to solve it. We use an eighth-order Runge–Kutta method as implemented in

the PYTHON package SCIPY to integrate the differential equation and obtain the density solutions. To integrate equation (5), we need to know the *'initial condition'* or the values of $\frac{\partial \rho_i}{\partial z}$ and ρ_i at $z = 0$, from where we start the integration. We can adopt

$$(\rho_i)_{z=0} = \rho_{i,0} \quad \text{and} \quad \left(\frac{\partial \rho_i}{\partial z}\right)_{z=0} = 0 \qquad (9)$$

Due to vertical symmetry, the density at the mid-plane is expected to be maximum, leading to the second condition. However, for the first condition, one needs to know the mid-plane density at every radius to initiate the integration. However, this midplane density is not a directly measurable quantity in galaxies (except for the Galaxy, see e.g. Kalberla & Dedes 2008; Grabelsky et al. 1987, 1988; Wouterloot et al. 1990; López-Corredoira & Molgó 2014; Wang et al. 2018). We estimate this mid-plane density at every radius using the knowledge of the surface densities at that radius.

Adopting a similar strategy as used by many previous authors (Narayan & Jog 2002; Banerjee et al. 2011; Patra et al. 2014; Patra 2018, 2019), we use an iterative approach to find the mid-plane density using the knowledge of the observed surface density. For solving at a particular radius for a particular component, say, stars, we first assume a trial mid-plane density $\rho_{i,0,t}$, and solve equation (5). This will result in a trial solution $\rho_{i,t}(z)$. This solution is not the correct solution as we chose the $\rho_{i,0,t}$ arbitrarily. Now, we can integrate this solution, to obtain a trial surface density as $\Sigma_{i,t} = 2 \times \int_0^\infty \rho_{i,t}(z)dz$. The surface density is an observable quantity at every radius and can be compared with the trial one $(\Sigma_{i,t})$ to constrain the mid-plane density. We iteratively update the $\rho_{i,0,t}$, such as it produces a $\Sigma_{i,t}$ close to the observation. We stop this iterative process when the trial surface density matches the observed one with better than 0.1 per cent accuracy. For our sample galaxies, we find that the surface densities for any component converge within 10s of iterations at any radius. It should be mentioned here that we assumed the observed column density at any radius is fully determined by the vertical density distribution at that radius. For an H I disc with finite thickness, this will only be true for a face-on orientation. In any other inclination, the density distribution of the adjacent radii would contribute to the surface density. However, the error introduced due to this effect is expected to be smaller as compared to the observational uncertainties.

Equation (5) represents three coupled differential equations (for three baryonic discs), and hence, in principle, should be solved simultaneously. This is not possible as the exact mathematical form of the coupling between the components is not known. Hence, we adopt an iterative approach to introduce the coupling gradually while solving the equations individually. At any radius, we first solve the three equations (for three components) separately, considering no coupling. For example, in the first iteration, in the gravity term (first term in the RHS of equation 5), we make $\rho_i = 0$ for all the components except the one we are solving for. In the next iteration onwards, we introduce the gravity of the components through the coupling term. For example, in the first iteration, when we solve for stars, we consider $\rho_{HI} = \rho_{H2} = 0$, that is, no coupling. Thus we generate a primary solution $\rho_{s,1}(z)$ for the stars. The second index in the subscript represents the iteration number. Similarly, we generate solutions for H I and H_2, $\rho_{HI,1}$ and $\rho_{H2,1}$. In the next iteration, we introduce $\rho_{HI,1}$ and $\rho_{H2,1}$ in the gravity term while solving for stars and generate a solution $\rho_{s,2}(z)$. Now, this is a better solution than what is obtained in the first iteration as it includes the gravity of H I and H_2 while solving for stars. Similarly, we obtain $\rho_{HI,2}$ and $\rho_{H2,2}$ at the end of the second iteration. However, as $\rho_{HI,1}$ and $\rho_{H2,1}$ was not perfect; these solutions are also not perfect but better than
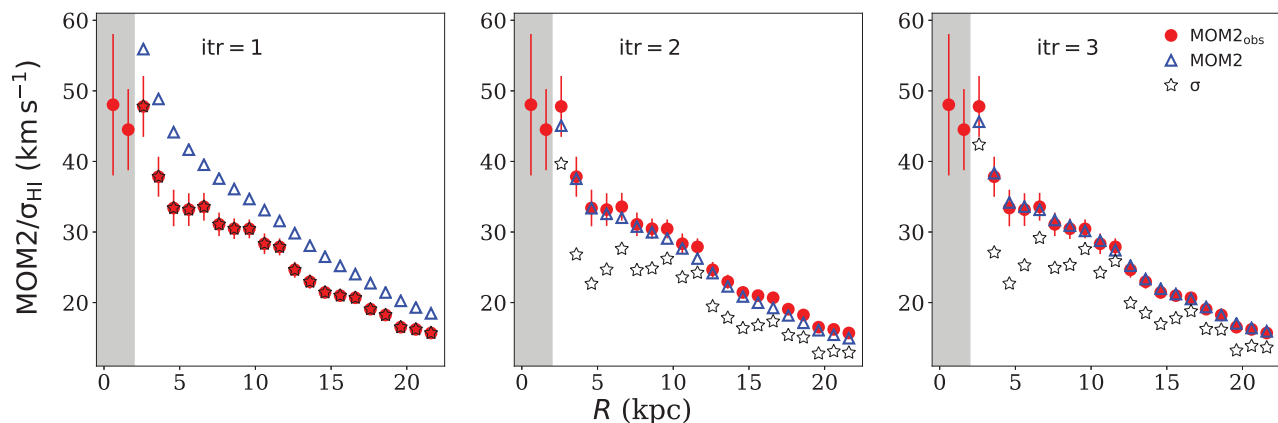
Figure 4. The σ/MOM2 profile of NGC 7331 at different iterations of the iterative method. The solid red circles with error bars in each panel represent the observed MOM2 profile. The empty black stars represent the input σ_{HI} profile, whereas the empty blue triangles represent the corresponding simulated MOM2 profiles. The iteration numbers every panel represents are quoted on the top left of every panel. As can be seen, the iterative method gradually finds out a σ_{HI} profile, which produces an MOM2 profile much close to the observed one. The shaded regions in each panel represent the radius where the iterative method is not applied due to high spectral blending. See the text for more details.

what was obtained in the first iteration. The consecutive iterations are thus run with improved coupled solutions. We repeat this process until the solutions converge, that is there is no effective difference between $\rho_{i, n}(z)$ and $\rho_{i, n-1}(z)$, where n is the number of iteration. We note that for our sample galaxies, the coupling quickly converges within a few iterations.

As mentioned earlier, to solve equation (5); often, the observed MOM2 is used as a proxy for σ_{HI}. However, MOM2 is always an overestimate of the σ_{HI} due to various smearing effects. To overcome this, we employ an iterative method to estimate the intrinsic σ_{HI} profile using the observed MOM2 in galaxies. In the first iteration of this method, we assume the observed MOM2 profile (M2$_{obs}$) to be the input H I velocity dispersion profile, $\sigma_{HI, 1}$ and solve equation (5). Thus, we generate the density solutions for H I, $\rho_{HI}(R, z)$. This $\rho_{HI}(R, z)$ describes a complete 3D distribution of the H I in a galaxy. Using this $\rho_{HI}(R, z)$ and the observed rotation curve, we then build a 3D dynamical model of the galaxy. We then incline this 3D dynamical model to the observed inclination and project it into the sky plane to obtain an H I spectral cube sampled with the same velocity resolution as of the observation [1.3 km s^{-1} (one galaxy) or 2.6 km s^{-1} (one galaxy) or 5.2 km s^{-1} (five galaxies) for our sample galaxies]. This spectral cube further convolved to the telescope beam to mimic the actual observation. The spectral cube then used to produce the moment maps and hence, a simulated MOM2 profile, M2$_{sim, 1}$. In an ideal situation, if the $\sigma_{HI, 1}$ was chosen perfectly, the M2$_{sim, 1}$ would match the observed MOM2 profile, M2$_{obs}$. However, as the MOM2 is an overestimate of the intrinsic σ_{HI}, M2$_{sim, 1}$ > M2$_{obs}$.

Next, we compute the difference between M2$_{sim, 1}$ and M2$_{obs}$ at every radius and introduce a proportional change into the input σ_{HI} for the next iteration $\sigma_{HI, 2}$. Thus, $\sigma_{HI, 2}$ is a better estimate of the σ_{HI}, which will produce an M2$_{sim, 2}$ closer to M2$_{obs}$ than what was found in the previous iteration. We continue this process until the difference between the observed and the simulated MOM2 at any radius reduces below a few km s^{-1}, which is at least two times better than the velocity resolution of the observation. We note that for our sample galaxies, this method reaches the convergence criteria within a few iterations.

In Fig. 4, we show how the iterative method estimates a σ_{HI} profile, which produces the observed MOM2 profile for NGC 7331. In the left-fand panel, we show the first iteration where the observed

MOM2 profile (solid red circles with error bars) is taken as the input σ_{HI} profile (empty black stars). This produces a simulated MOM2 profile (empty blue triangles), which is higher than the observed one. In the next iteration, we introduce a proportional change in the input σ_{HI} profile, as shown in the middle panel. As can be seen, a lower input σ_{HI} profile now produces an MOM2 profile, which is closer to the observed one. In the right-hand panel, we show the results from the third iteration. The updated σ_{HI} profile in this iteration produces a MOM2 profile that matches the observed ones within our convergence criteria. It should be noted that the satisfaction of the hydrostatic equilibrium condition is crucial for our analysis. Any violation of the same might lead to a wrong interpretation of the results. Observationally, the central regions of spiral galaxies ($\lesssim$ 1 kpc) are generally found to exhibit highly energetic activities with associated outflows and enhanced star formation (Irwin & Sofue 1996; Bolatto et al. 2013). Subsequently, in these regions, the condition of hydrostatic equilibrium might not be valid fully. Moreover, due to several other effects, dor example, the high gradient in rotation curve, strong non-circular motions, etc., the H I spectra in these regions could be broadened by a significant amount. Such as, this artificial broadening dominates the spectral width (especially for high inclination galaxies) as compared to the actual σ_{HI}. Consequently, in these regions, the effective M2$_{sim}$ becomes insensitive to σ_{HI}, and the iterative method fails to recover the intrinsic σ_{HI} profiles effectively. Further, a high MOM2 value also leads to a divergence of equation (5) in the first iteration of the iterative method. Considering these complexities, we exclude a portion of the central regions (by a trial-and-error method) of our galaxies and do not apply the iterative method. The grey shaded areas in Figs 4 and 5, show the extent of these regions for our galaxies.

5 RESULTS AND DISCUSSION

We apply the above-mentioned iterative method in our seven sample galaxies and solve the hydrostatic equilibrium equation. In Fig. 5, we show how the iterative method estimates the σ_{HI} profiles in our galaxies using the observed MOM2 profiles. As can be seen from the figure, the iterative method could assess the σ_{HI} profiles, such as the output MOM2 profiles matches to the observed ones reasonably well. The inclinations and the spatial resolutions of the
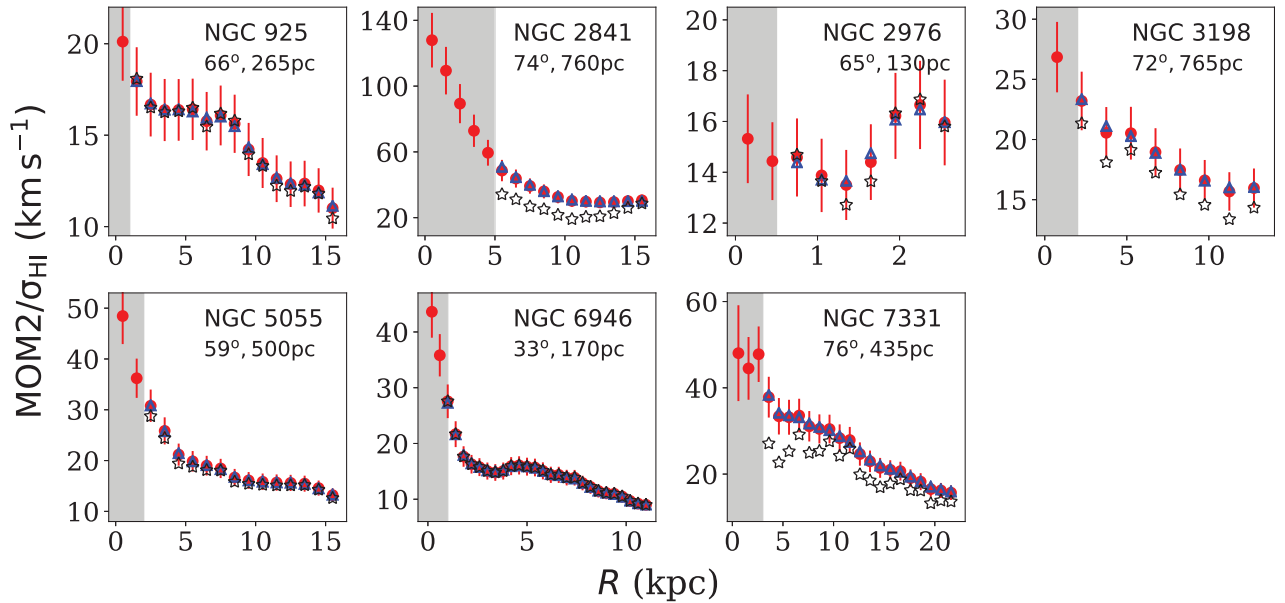
Figure 5. The σ_{HI}/MOM2 profiles of our sample galaxies as extracted by the iterative method. Different panels show the results for different galaxies, as quoted at the top of each panel. The solid red circles with error bars represent the observed MOM2, whereas the empty blue triangles represent the simulated MOM2. The input σ_{HI} is shown by the empty black stars. The inclinations and the spatial resolutions of the galaxies are also quoted at the top of every panel. As can be seen, highly inclined galaxies with low spatial resolution suffer maximum spectral blending as indicated by the difference between the recovered σ_{HI} and the observed MOM2. See the text for more details.

observations quoted at the top of every panel in Fig. 5. As can be seen, galaxies with high inclinations and coarse spatial resolutions (e.g. NGC 2841 and NGC 3521) exhibit maximum spectral blending, which in turn results in a maximum difference between the observed MOM2 profile and the estimated σ_{HI}. Galaxies with low inclinations and high spatial resolutions endure negligible or minimal blending. For example, NGC 6946 has an inclination of 33° and was observed with a spatial resolution of ∼170 pc. For this galaxy, the intrinsic σ_{HI} profile matches with the observed MOM2 profile well within a few per cent. This indicates, for this kind of observational parameters, the observed MOM2 represent the intrinsic σ_{HI} profile fairly well. This has a significant impact on understanding the connection between the velocity dispersion and various physical processes (e.g. star formation, feedback, etc.) in a galaxy.

Using a different approach, very recently, Bacchini et al. (2019a) had estimated the σ_{HI} profiles in a sample of 12 nearby galaxies. They used the H I spectral cubes to perform a rigorous 3D tilted-ring modelling using the software ^{3D}Barolo (Di Teodoro & Fraternali 2015) and simultaneously model the H I velocity dispersion (see also, Iorio et al. 2017). They used these σ_{HI} profiles to estimate the vertical scale height profiles of the H I discs employing a hydrostatic equilibrium condition. In Fig. 6, we compare our σ_{HI} profiles as estimated by the iterative method (black filled asterisks) to what is determined by Bacchini et al. (2019a, empty red squares). As can be seen from the figure, for most of our galaxies, both the σ_{HI} profiles match reasonably well. However, for the galaxy NGC 2841, the iterative method recovers much higher σ_{HI} values as compared to what is obtained by Bacchini et al. (2019a). The inclination of NGC 2841 is 74°, and it was observed with a coarse spatial (760 pc) and spectral resolutions (5.2 km s^{-1}). Its rotation curve also shows a significant gradient (Fig. 2, second panel on the top) across all radius. It is possible that significant smearing is introduced due to these effects, and in these circumstances, the iterative method might not be fully effective in recovering the σ_{HI} correctly. We also note

that the recovered σ_{HI} for the galaxy NGC 7331 is somewhat higher than what is observed for other galaxies in our sample (however, though it matches reasonably well with that of obtained by Bacchini et al. 2019a). This could also be due to its high inclination (76°) and a modest spatial resolution (∼450 pc). We emphasize that despite a completely different approach, our iterative method recovers σ_{HI} profiles, which are consistent with those found by Bacchini et al. (2019a).

Thus, for all our galaxies, using the iterative method, we self-consistently solve for the density distributions and the σ_{HI} profile. In Fig. 7, we plot a sample solution for NGC 7331 at a radius of 10 kpc. For comparison, we also plot the density solutions for an assumed constant $\sigma_{HI} = 12$ km s^{-1} at the same radius (thin lines). This $\sigma_{HI} = 12$ km s^{-1} is commonly used as the velocity dispersion of the H I discs in spiral galaxies as estimated by Caldú-Primo et al. (2013) and Mogotsi et al. (2016) using the THINGS data. As can be seen from the figure, a constant $\sigma_{HI} = 12$ km s^{-1} produces a very different H I disc as compared to what is found by the iterative method. The σ_{HI} found by the iterative method at a radius of 10 kpc is ∼ 28 km s^{-1} which is significantly higher than the constant $\sigma_{HI} = 12$ km s^{-1}. This higher σ_{HI} significantly flares the H I disc (at 10 kpc), resulting in a much larger H I scale height. However, though the σ_{HI} changes the H I density distribution significantly, it marginally influences the H_2 (dotted thin and thick blue lines) and the stellar discs (solid thin and thick red lines), as can be seen from the figure. We note that for a single-component isothermal disc in hydrostatic equilibrium, the density distribution follows a *sech*^{2} law (Spitzer 1942). However, for a galaxy with multiple discs and dark matter halo, the density distribution deviates significantly from *sech*^{2} law and resembles more like a Gaussian due to coupling (see e.g. Olling 1995; Koyama & Ostriker 2009).

We use the density solutions of our sample galaxies to extract the H I scale heights, the HWHM. In Fig. 8, we plot, thus, obtained H I scale height profiles (thick blue lines) along with the estimated
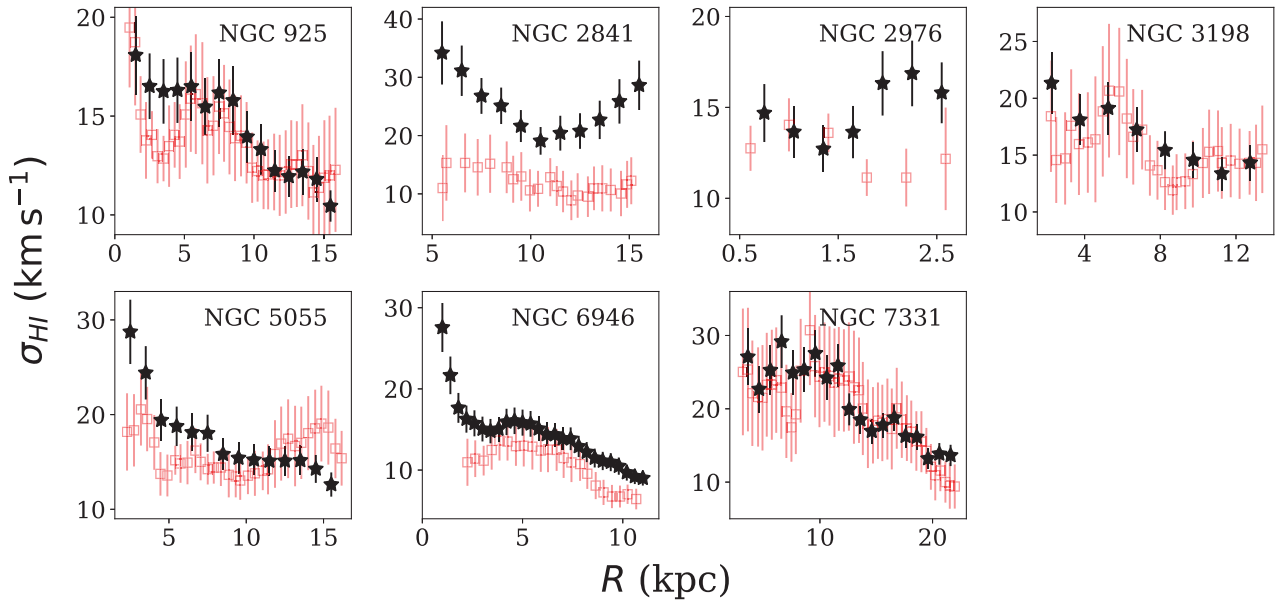
Figure 6. Comparison of our $\sigma_{\rm HI}$ profiles to the same as obtained by Bacchini et al. (2019a). The solid black asterisks represent the $\sigma_{\rm HI}$ profiles as recovered by the iterative method, whereas the empty red squares indicate the $\sigma_{\rm HI}$ profiles as determined by Bacchini et al. (2019a). As can be seen, for most of the galaxies, both the $\sigma_{\rm HI}$ profiles match each other reasonably well. See the text for more details.
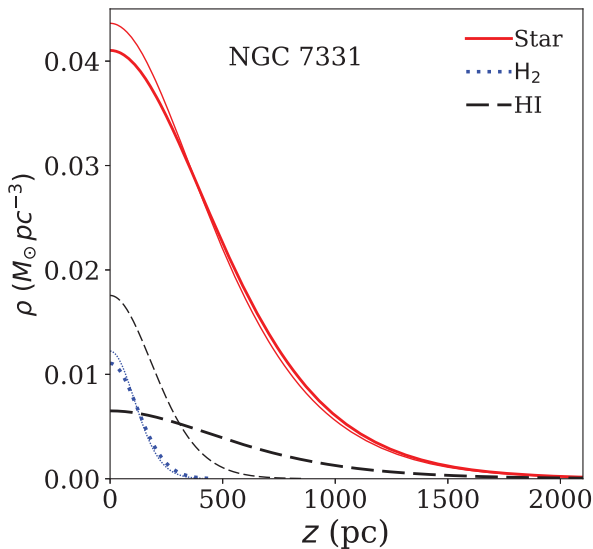

Figure 7. The sample solution for NGC 7331 at a radius of 10 kpc. The thick lines represent the solutions using our iterative method (with recovered $\sigma_{\rm HI}$), while the thin lines represent the solutions assuming a constant $\sigma_{\rm HI} = 12$ km s^{-1}. The solid red lines describe the volume density of stars, whereas the blue dotted lines represent the density of molecular gas. The black dashed lines denote the solutions for H I. As can be seen, a constant velocity dispersion for H I produces a very different H I disc than what would be otherwise. See the text for more details.

errors on them (blue shaded region). For comparison, in every panel, we also plot the H I scale height profiles obtained by Bacchini et al. (2019a, red shaded region). As can be seen, for most of the galaxies, both the H I scale height profiles compare well to each other. For NGC 2841 and NGC 6946, however, the scale height profiles differ considerably from what is obtained by Bacchini et al. (2019a). This could be attributed to the difference in their $\sigma_{\rm HI}$ profiles, as compared to what is obtained by Bacchini et al. (2019a) (Fig. 6,

second and sixth panels). As can also be seen in Fig. 8, the H I discs in our sample galaxies flares as a function of radius. However, the nature of the flaring is not uniform, and the shape of the scale height profiles vary across our sample galaxies. To quantify this flaring further, we fit these H I scale height profiles with straight lines (shown by the black dashed lines). We note that the variation of the shape of the scale height profiles across the galaxies is significant, and hence a simple linear fit is employed to describe the profiles reasonably. The respective slope and the intercepts of the fits are quoted at the top left of corners of the individual panels.

To further investigate the global behaviour of the H I flaring in our sample galaxies, we normalize the H I scale height profiles to unity at a radius of $0.3r_{25}$, where r_{25} is the optical radius of a galaxy calculated by fitting 25th magnitude isophote in *B* band. Schruba et al. (2011) had used the same normalizing condition to find a universality in the H_2 surface density profiles in spiral galaxies. Further, Patra (2019) used the same condition to normalize the H_2 scale height profiles in spiral galaxies. Their results suggest a global dependence of the molecular surface density/scale height on the characteristic stellar surface density distribution in a galaxy. In Fig. 9, we plot the normalized H I scale height profiles (solid grey lines) for our sample galaxies. As can be seen, despite having a substantial scatter in the normalized scale height profiles, they seem to follow a reasonably well linear trend. This indicates that, globally, the normalized scale height profiles follow a universal linear law. To quantify this flaring behaviour further, we evaluate a bin average of these normalized scale heights within a radial bin of $0.1\ r_{25}$ (blue squares with error bars) and fit it with a straight line (red dashed line). We find a slope of 1.84 ± 0.12 and an intercept of 0.53 ± 0.04. We note that our normalized scale height profiles exhibit a significantly higher scatter than what is found by Patra (2019) for molecular scale heights. This indicates a weaker global dependence of the H I scale height on the stellar surface density profiles.

The H I scale height serves as an indicator of the thickness/density distribution in the vertical direction of the H I disc. As can be seen in
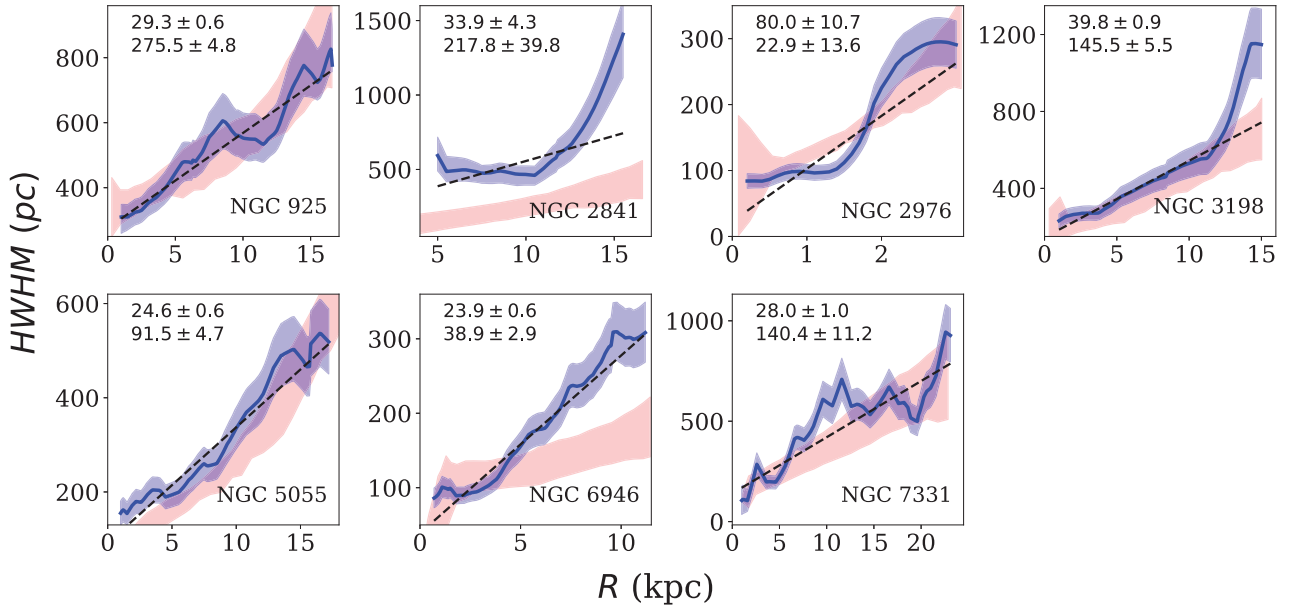
Figure 8. The H I scale height (HWHM) profiles of our sample galaxies. Different panels represent the scale heights for different galaxies, as quoted in the bottom right corners of every panel. The thick blue lines represent the H I scale height profiles, whereas the blue-shaded regions depict its 1σ error bar. The black dashed lines represent a linear fit to these scale height profiles. The two numbers from the top left of every panel indicate the slopes (in the units of pc/kpc) and the intercepts (in the units of pc) of the fitted lines, respectively. The red shaded region in every panel represents the H I scale height profiles obtained by Bacchini et al. (2019a). As can be seen, for most of the galaxies, our determination of the scale heights compares very well with what is found by Bacchini et al. (2019a). See the text for more details.
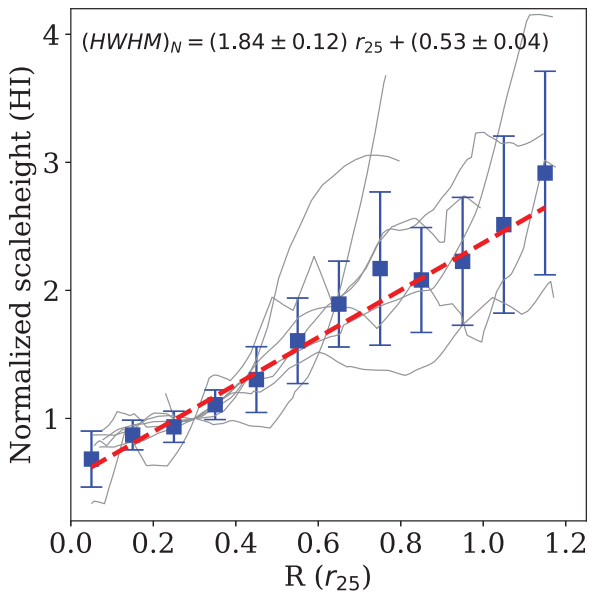

Figure 9. The normalized scale height profiles of our sample galaxies. The thin grey lines represent the normalized scale height profiles, whereas the solid blue squares with error bars represent the average normalized scale height values within a bin of width 0.1 r_{25}. The red dashed line represents a linear fit to these average normalized scale heights. The corresponding straight line equation is quoted at the top left of the figure. See the text for more details.

Fig. 8, the H I scale height in our sample galaxies varies between a few hundred parsecs in the central region (within a few kpc) to ~1–2 kpc at the outskirts of the H I discs. This thickness is comparable to that of the Galaxy (see e.g. Kalberla & Dedes 2008; Bacchini et al.

2019b) and is much smaller as compared to what is found in dwarf galaxies by a similar analysis (Patra 2020a). This indicates that the H I discs in spiral galaxies are much thinner as compared to the dwarf galaxies.

To make a better sense of the relative thickness of the H I discs in our sample galaxies, we estimate the axial ratios using the scale height data. We define the axial ratio as the ratio of the maximum thickness of the H I disc (taken to be two times the FWHM$_{max}$) to the diameter of the H I disc, D_{max}. As FWHM (full width at half-maximum) represents only half of the maximum density, we use two times the FWHM (to account for the wings of the Gaussian) as a conservative limit to the maximum H I thickness. This ratio is an indicator of the relative thickness of the H I discs, which can be compared with other galaxies. In Fig. 10, we plot the axial ratios of our sample galaxies. The axial ratio varies from ~0.06 to ~0.22 with a median value of 0.1 (blue dashed line). This median value is very close to the axial ratio found for the Milky Way (Kalberla & Dedes 2008), which is ~0.13 (black dashed–dotted line). Interestingly, there are three galaxies in our sample, that is, NGC 5055, NGC 6946, and NGC 7331, for which the axial ratios are much less than 0.1. An axial ratio of $\lesssim 0.1$ for the optical discs in galaxies is traditionally considered an indicator of a superthin galaxy (Goad & Roberts 1981; Karachentsev, Karachentseva & Parnovskij 1993; Karachentsev, Karachentseva & Kudrya 1999). However, though there is no clear assessment of the axial ratios of the H I discs to qualify a galaxy to be superthin, we adopt the same ratio used for the optical discs as a conservative limit. For example, by performing a detailed 3D modelling, Matthews & Wood (2003) estimated the H I scale heights in UGC 7321, a well-known superthin galaxy. For this galaxy, the axial ratio of the H I disc is found to be 0.07, whereas we find axial ratios of 0.06, 0.06, and 0.08 for NGC 5055, NGC 6946, and NGC 7331, respectively. Mass modelling of superthin galaxies also revealed that the superthin galaxies host a compact
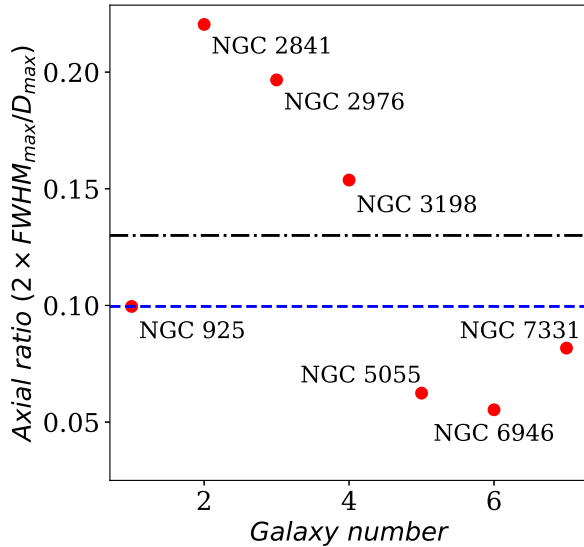
Figure 10. The axial ratio of our sample galaxies. Axial ratio is defined as the ratio of twice the FWHM of H I distribution to the H I diameter of a galaxy. The solid red circles represent the axial ratio for our sample galaxies. The blue dashed line represents the median axial ratio, whereas the black dashed–dotted line represents the same for the Milky Way. As can be seen, the median axial ratio of our sample galaxies matches closely to that of the Galaxy. See the text for more details.

dark matter halo with $R_C/R_D < 2$, where R_C is the core radius of the dark matter halo and R_D is the scale length of the optical disc (see e.g. Banerjee & Bapat 2017). For our three galaxies, R_C/R_D are found to be 3.7, 1.6, and 1.4 for NGC 5055, NGC 6946, and NGC 7331, respectively. As can be seen, except NGC 5055, the other two galaxies host compact dark matter haloes as well. These results suggest that NGC 5055, NGC 6946, and NGC 7331 could possibly represent superthin galaxies. However, detailed comparisons of other physical properties and an edge-on projected view of the baryonic discs would be necessary to make any firm conclusion.

The thickness of the H I discs in galaxies has many significant implications. For example, a thin disc offers a much smaller cross-section to the background quasars to produce H I absorption spectra. The thickness of the H I discs very often decides the sizes of the H I shells or holes forms out of star formation feedback/supernovae. For example, Boomsma et al. (2008) detected a large number of H I holes and high-velocity gas in the typical spiral galaxy NGC 6946 (which is also present in our sample galaxy). They found the average diameter of the H I holes to be 1.2 kpc, whereas the diameter of the smallest hole is 766 pc. For NGC 6946, we find that the H I scale height reaches up to ∼300 pc at a radius of ∼ 12 kpc. This means that the thickness of the H I disc in NGC 6946 cannot contain the H I holes entirely, and most probably, they have broken out into the immediate environment of the CGM.

To further investigate the effectiveness of the H I holes in NGC 6946 in breaking out into the CGM, we calculate the fractional H I density at the edge of the H I holes in the vertical direction. To do that, we use the size and the location of the detected H I holes in NGC 6946 from Boomsma (2007). Using our solution at the radius where the H I hole is detected, we calculate the volume density of H I ($\rho_{HI, B}$) at a height equal to the radius of the hole. Using this $\rho_{HI, B}$, and the mid-plane density at that radius, we determine the density fraction. This can be thought of as the fraction of the mid-plane density at the edge of the H I hole in the vertical direction. In the top panel
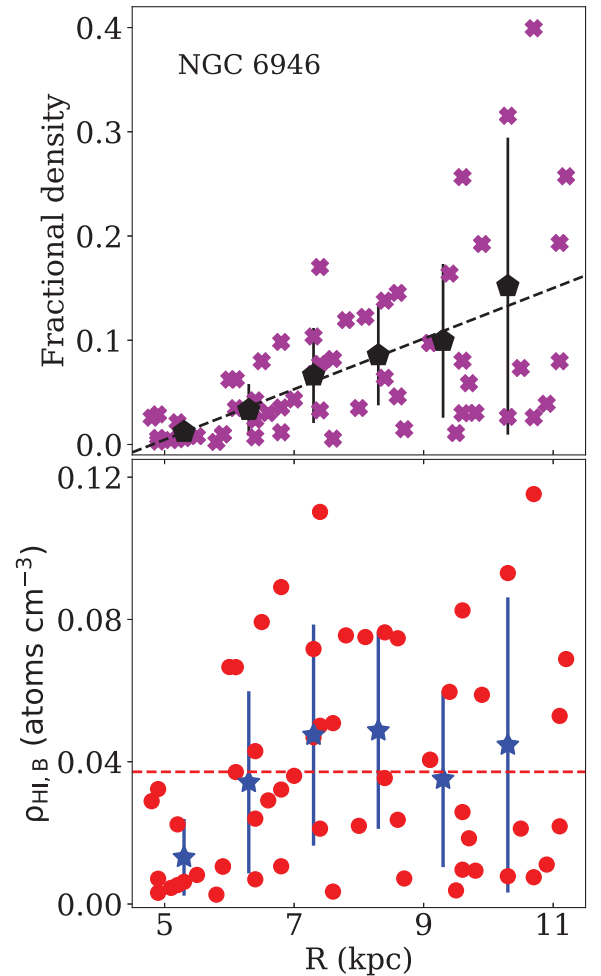
Figure 11. Top panel: the fraction of the mid-plane density at a height equal to the radius of an H I hole. The thick magenta crosses represent the fraction, whereas the black pentagons with error bars represent average values within a radial bin of 1 kpc. The black dashed line represents a linear fit to the bin averaged values. See the text for more details. Bottom panel: the solid red circles represent the volume density of the H I at a height equal to the radius of an H I hole. The blue stars with error bars represent the average values of the same within a radial bin of 1 kpc. The red dashed line represents the mean particle density when an H I hole breaks out. See the text for more details.

of Fig. 11, we plot this fraction for all the H I holes in NGC 6946 as a function of radius. As can be seen from the figure, for all the holes, the fraction remains less than 0.5, the density point defining the scale height. The majority number of holes have a density fraction of less than 0.2. This means the holes reach much lower densities as compared to the mid-plane density, strongly indicating a breakout of the H I holes into the CGM. As also can be seen from the figure, the density fraction increases as a function of the radius with very low values at the inner galaxies. This indicates that the H I holes are more effective in polluting CGM at inner radii as compared to outer radii. To quantify this linear increase, we evaluate an average bin value (black pentagons) withing a radial bin of 1 kpc and fit these average values with a straight line (black dashed line). We find a slope of 0.024 ± 0.001 and an intercept of −0.117 ± 0.007 for the linear fit. We would like to mention here that for this analysis, we exclude H I holes in a region where we do not solve the hydrostatic equation.

Next, in the bottom panel of Fig. 11, we plot the particle density at the edge of the H I holes (in the vertical direction) as a function

of radius. As can be seen from the figure, the $\rho_{HI, B}$ vary between $\sim 0.03 - 0.1$ atoms cm^{-3} with a mean value of 0.04 atoms cm^{-3}. We further calculate the average values of this breakout density within radial bins of 1 kpc (shown by the blue filled stars with error bars) and found them to be reasonably constant as a function of radius. However, given the uncertainty, this result is only indicative, and a more detailed study is necessary to draw firm conclusions.

6 CONCLUSION

In summary, we model galactic discs to be three-component systems consisting of stars, molecular gas, and atomic gas in vertical hydrostatic equilibrium. Under this assumption, we set up the Poisson–Boltzmann equation of hydrostatic equilibrium in a sample of seven large spiral galaxies from the THINGS survey. We solve the hydrostatic equations numerically using an eighth-order Runge–Kutta method to estimate the 3D distribution of the H I in our sample galaxies.

The H I velocity dispersion, σ_{HI}, is one of the critical inputs which directly influences the vertical distribution of the H I in a galaxy. We do not assume the σ_{HI} to be constant across our sample or within a galaxy. Instead, we develop an iterative method by which we use the observed MOM2 profile in a galaxy to estimate its intrinsic σ_{HI} profile. We find that the iterative method estimates the σ_{HI} profiles in our galaxies reasonably well, such as the output MOM2 profiles match the observation within a few per cents. Our method self-consistently computes the σ_{HI} profile for a galaxy, which is not possible to directly estimate due to line-of-sight integration effects.

Using this iterative method, we solve the hydrostatic equilibrium equation to obtain a detailed 3D distribution of the H I in our sample galaxies. Our method reveals that though a constant $\sigma_{HI} = 12$ km s^{-1} does not affect the density distribution of the stars and the molecular gas considerably, it alters the distribution of the H I in a significant way. Hence, a precise estimation of the σ_{HI} is essential to determine the distribution of H I in galaxies accurately. From the solutions of the hydrostatic equation, we also find that due to coupling between the disc components and the presence of the dark matter halo, the density of different disc components deviates from the traditional *sech*^{2} law and behaves more like a Gaussian function as also found by previous studies.

Using the density solutions for the H I disc, we estimate the H I scale heights (HWHM) in our sample galaxies. We find that the H I scale height increases as a function of radius, that is, the H I disc flares. This flaring can be represented reasonably well by a linear increase. The scale height of the H I discs in our sample galaxies are found to vary between a few hundred parsecs at the centre to ∼1–2 kpc at the edge of the H I discs. This scale height is much lower as compared to what is observed in dwarf galaxies, indicating thinner H I discs in spiral galaxies.

We further investigate the universality of the H I flaring in our galaxies by normalizing the H I scale height profiles to unity at a radius of 0.3 r_{25}. Despite a considerable variation in the individual scale height profiles, the normalized profiles are found to follow a linear behaviour with a slope of 1.84 ± 0.12 and an intercept of 0.53 ± 0.04. The scatter in the normalized H I scale height profiles are found to be much higher than what is observed for the molecular scale height profiles. This indicates a weaker global dependence of H I scale height on the stellar surface density profiles.

We quantify the thickness of the H I discs in our sample galaxies by estimating an axial ratio, the ratio of two times the maximum FWHM of the H I distribution to the H I diameter of a galaxy. This axial ratio serves as a measure of the thickness of the H I discs in

galaxies. We find that the axial ratios for the H I discs in our galaxies vary between ~ 0.06 and 0.22 with a median of ~ 0.1. This median axial ratio is very close to what is found for the Milky Way and is much less than what is found for the dwarf galaxies. Using this axial ratio as an indicator, we identify three galaxies in our sample, that is, NGC 5055, NGC 6946, and NGC 7331 as potential candidates for superthin galaxies.

We use the 3D density distribution of H I in one of our sample galaxies, NGC 6946, to estimate the volume density as a fraction of the mid-plane density at the edge of the H I holes (in the vertical direction) as detected by Boomsma et al. (2008). We find that most of the H I holes reach a density, which is $\lesssim 10 - 20$ per cent of the mid-plane density. This indicates that most of the H I holes in NGC 6946 are broken into the CGM. We also find a linear increase of this fraction as a function of radius, meaning a more efficient metal mixing in the IGM in the inner galaxy as compared to the outer galaxy. We also measure the volume density of H I at the edge of the H I holes (breakout density) and find a mean value of 0.04 atoms cm^{-3}. Despite considerable variation in this breakout density amongst the holes, the bin averaged values seem to be reasonably constant as a function of radius. This further strengthens the possibility that the holes are broken out into the CGM.

Our study points out that it is vital to determine the vertical thickness and the distribution of H I accurately in galaxies to understand various physical processes that influence its evolution. Our iterative method offers a simultaneous estimation of the σ_{HI} and the H I distribution in a self-consistent manner. Given the observing parameters, our method can be used to estimate the amount of spectral blending in a galaxy, which can play a crucial role in interpreting H I spectral data.

DATA AVAILABILITY

We used already existing publicly available data for this work. No new data were generated or analysed in support of this research. The scale height and the σ_{HI} profiles are available from the author on a reasonable request.

REFERENCES

Abramova O. V., Zasov A. V., 2008, Astron. Rep., 52, 257
Alves J., Lombardi M., Lada C. J., 2007, A&A, 462, L17
Bacchini C., Fraternali F., Iorio G., Pezzulli G., 2019a, A&A, 622, A64
Bacchini C., Fraternali F., Pezzulli G., Marasco A., Iorio G., Nipoti C., 2019b, A&A, 632, A127
Bahcall J. N., 1984a, ApJ, 276, 169
Bahcall J. N., 1984b, ApJ, 276, 156
Bahcall J. N., Casertano S., 1984, ApJ, 284, L35
Bahcall J., Flynn C., Gould A., 1991, in Sundelius, B., ed., Dynamics of Disc Galaxies, Dept. Astron. Astrophys., Chalmers Univ. of Technology, Göteborg, p. 105
Banerjee A., Bapat D., 2017, MNRAS, 466, 3753
Banerjee A., Jog C. J., 2008, ApJ, 685, 254
Banerjee A., Matthews L. D., Jog C. J., 2010, New Astron., 15, 89
Banerjee A., Jog C. J., Brinks E., Bagetakos I., 2011, MNRAS, 415, 687

Begeman K. G., 1987, PhD thesis. Kapteyn Institute

Bigiel F., Leroy A., Walter F., Brinks E., de Blok W. J. G., Madore B., Thornley M. D., 2008, AJ, 136, 2846

Bolatto A. D. et al., 2013, Nature, 499, 450

Boomsma R., 2007, PhD thesis. Kapteyn Astronomical Institute, University of Groningen

Boomsma R., Oosterloo T. A., Fraternali F., van der Hulst J. M., Sancisi R., 2008, A&A, 490, 555

Bosma A., 1978, PhD thesis, University of Groningen

Bosma A., 1981, AJ, 86, 1825

Brandt J. C., 1960, ApJ, 131, 293

Burton M. G., 1987, PhD thesis, University of Edinburgh

Caldú-Primo A., Schruba A., Walter F., Leroy A., Sandstrom K., de Blok W. J. G., Ianjamasimanana R., Mogotsi K. M., 2013, AJ, 146, 150

de Blok W. J. G., Walter F., Brinks E., Trachternach C., Oh S.-H., Kennicutt R. C., Jr, 2008, AJ, 136, 2648

Di Teodoro E. M., Fraternali F., 2015, MNRAS, 451, 3021

Goad J. W., Roberts M. S., 1981, ApJ, 250, 79

Grabelsky D. A., Cohen R. S., Bronfman L., Thaddeus P., May J., 1987, ApJ, 315, 122

Grabelsky D. A., Cohen R. S., Bronfman L., Thaddeus P., 1988, ApJ, 331, 181

Iorio G., Fraternali F., Nipoti C., Di Teodoro E., Read J. I., Battaglia G., 2017, MNRAS, 466, 4159

Irwin J. A., Sofue Y., 1996, ApJ, 464, 738

Kalberla P. M. W., Dedes L., 2008, A&A, 487, 951

Kamphuis J., Sancisi R., 1993, A&A, 273, L31

Karachentsev I. D., Karachentseva V. E., Parnovskij S. L., 1993, Astron. Nachr., 314, 97

Karachentsev I. D., Karachentseva V. E., Kudrya Y. N., 1999, Astron. Lett., 25, 1

Kennicutt R. C., Jr, 1998, ApJ, 498, 541

Kennicutt R. C., Jr, et al., 2003, PASP, 115, 928

Koyama H., Ostriker E. C., 2009, ApJ, 693, 1346

Leroy A. K. et al., 2009, ApJ, 702, 352

Leroy A. K., Walter F., Brinks E., Bigiel F., de Blok W. J. G., Madore B., Thornley M. D., 2008, AJ, 136, 2782

López-Corredoira M., Molgó J., 2014, A&A, 567, A106

Mac Low M.-M., Ferrara A., 1999, ApJ, 513, 142

Madore B. F., 1977, MNRAS, 178, 1

Marasco A., Fraternali F., van der Hulst J. M., Oosterloo T., 2017, A&A, 607, A106

Matthews L. D., Wood K., 2003, ApJ, 593, 721

Mogotsi K. M., de Blok W. J. G., Caldú-Primo A., Walter F., Ianjamasimanana R., Leroy A. K., 2016, AJ, 151, 15

Nakanishi H., Sofue Y., 2003, PASJ, 55, 191

Narayan C. A., Jog C. J., 2002, A&A, 394, 89

Oh S.-H. et al., 2015, AJ, 149, 180

Olling R. P., 1995, AJ, 110, 591

Patra N. N., 2018, MNRAS, 478, 4931

Patra N. N., 2019, MNRAS, 484, 81

Patra N. N., 2020a, MNRAS, 495, 2867

Patra N. N., 2020b, A&A, 638, A66

Patra N. N., Chengalur J. N., Begum A., 2013, MNRAS, 429, 1596

Patra N. N., Banerjee A., Chengalur J. N., Begum A., 2014, MNRAS, 445, 1424

Patra N. N., Chengalur J. N., Karachentsev I. D., Kaisin S. S., Begum A., 2016, MNRAS, 456, 2467

Rathborne J. M., Johnson A. M., Jackson J. M., Shah R. Y., Simon R., 2009, ApJS, 182, 131

Roman-Duval J., Jackson J. M., Heyer M., Rathborne J., Simon R., 2010, ApJ, 723, 492

Roman-Duval J., Heyer M., Brunt C. M., Clark P., Klessen R., Shetty R., 2016, ApJ, 818, 144

Romeo A. B., 1992, MNRAS, 256, 307

Roy N., Mathur S., Gajjar V., Patra N. N., 2013, MNRAS, 436, L94

Roychowdhury S., Chengalur J. N., Begum A., Karachentsev I. D., 2009, MNRAS, 397, 1435

Roychowdhury S., Huang M.-L., Kauffmann G., Wang J., Chengalur J. N., 2015, MNRAS, 449, 3700

Sarkar S., Jog C. J., 2018, A&A, 617, A142

Sarkar S., Jog C. J., 2019, A&A, 628, A58

Schruba A. et al., 2011, AJ, 142, 37

Shostak G. S., van der Kruit P. C., 1984, A&A, 132, 20

Silich S., Tenorio-Tagle G., 2001, ApJ, 552, 91

Sofue Y., 2017, PASJ, 69, R1

Spitzer L., Jr, 1942, ApJ, 95, 329

Stark A. A., 1984, ApJ, 281, 624

Tamburro D., Rix H.-W., Leroy A. K., Mac Low M.-M., Walter F., Kennicutt R. C., Brinks E., de Blok W. J. G., 2009, AJ, 137, 4424

Toomre A., 1964, ApJ, 139, 1217

van Albada T. S., Bahcall J. N., Begeman K., Sancisi R., 1985, ApJ, 295, 305

van der Kruit P. C., 1981, A&A, 99, 298

van der Kruit P. C., Searle L., 1981a, A&A, 95, 105

van der Kruit P. C., Searle L., 1981b, A&A, 95, 116

van der Kruit P. C., Shostak G. S., 1984, A&A, 134, 258

Walter F., Brinks E., de Blok W. J. G., Bigiel F., Kennicutt R. C., Jr, Thornley M. D., Leroy A., 2008, AJ, 136, 2563

Wang H.-F., Liu C., Xu Y., Wan J.-C., Deng L., 2018, MNRAS, 478, 3367

Wolfire M. G., McKee C. F., Hollenbach D., Tielens A. G. G. M., 1995, ApJ, 453, 673

Woolley R. V. D. R., 1957, MNRAS, 117, 198

Wouterloot J. G. A., Brand J., Burton W. B., Kwee K. K., 1990, A&A, 230, 21

Zwaan M. A., van der Hulst J. M., Briggs F. H., Verheijen M. A. W., Ryan-Weber E. V., 2005, MNRAS, 364, 1467

This paper has been typeset from a TEX/LATEX file prepared by the author.